iScience

CellPress
OPEN ACCESS

Article

The role of thermodynamically stable configuration in enhancing crystallographic diffraction quality of flexible MOFs

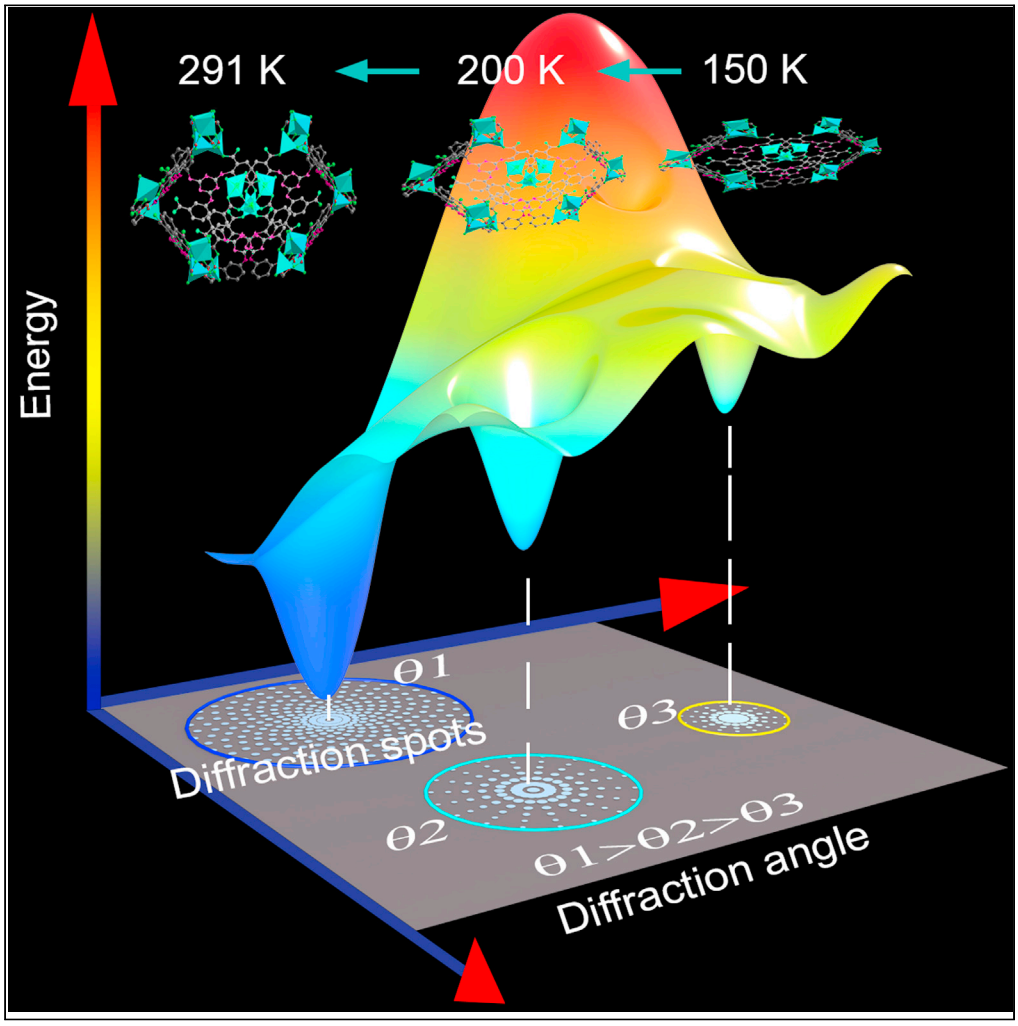

He Zhao, Jiaxiang Huang, Pei-Pei Zhang, ..., Xue-Dan Song, Shuqin Liu, Chunying Duan

zhangjj@dlut.edu.cn (J.-J.Z.)
cyduan@dlut.edu.cn (C.D.)

Highlights

A higher diffraction quality of single crystal at a higher temperature

An MOF with reversible anisotropic thermal expansion behavior

A more stable thermodynamic configuration improves the diffraction quality of crystal

Zhao et al., iScience 24, 103398
December 17, 2021
https://doi.org/10.1016/j.isci.2021.103398

iScience

CellPress
OPEN ACCESS

Article

The role of thermodynamically stable configuration in enhancing crystallographic diffraction quality of flexible MOFs

He Zhao,[1,2] Jiaxiang Huang,[2] Pei-Pei Zhang,[2] Jian-Jun Zhang,[1,2,4,*] Wang-Jian Fang,[2] Xue-Dan Song,[2] Shuqin Liu,[2] and Chunying Duan[1,3,*]

SUMMARY

Single-crystal X-ray diffraction (SCXRD) is a widely used method for structural characterization. Generally, low temperature is of great significance for improving the crystallographic diffraction quality. Herein we observe that this practice is not always effective for flexible metal-organic frameworks (*f*-MOFs). An abnormal crystallography, that is, more diffraction spots at a high angle and better resolution of diffraction data as the temperature increases in the *f*-MOF (1-g), is observed. XRD results reveal that 1-g has a reversible anisotropic thermal expansion behavior with a record-high *c-axial* positive expansion coefficient of 1,401.8 × 10^{-6} K^{-1}. Calculation results indicate that the framework of 1-g has a more stable thermodynamic configuration as the temperature increases. Such configuration has lower-frequency vibration and may play a key role in promoting higher Bragg diffraction quality at room temperature. This work is of great significance for how to obtain high-quality SCXRD diffraction data.

INTRODUCTION

Single-crystal X-ray diffraction (SCXRD), especially its in-house version, is becoming the most powerful, convenient, and economic technique for the structural study of crystalline samples at the atomic scale since W. L. Bragg finished the first structure solution of NaCl (Bragg and Bragg, 1913; Huang et al., 2021; Perles, 2020). So far, the application of this technology has been extended to many disciplines (Günther et al., 2021; Wang et al., 2020), especially for the single-crystal structure analyses of small molecules and biomacromolecules (Renaud et al., 2016; Yao et al., 2019) as well as metal-organic frameworks (MOFs) (Deng et al., 2012; Park et al., 2017; Rosi et al., 2003). Low temperature is an indispensable factor of this technology. It can usually suppress the thermal disorder of atoms to improve the diffraction quality of the data, thereby contributing to a clear atomic-scale structure (Goeta and Howard, 2004; Howard and Probert, 2014; Lee et al., 2014). However, this rule is not fully applicable in the MOF field. The pioneering work of Yaghi et al. shows that the diffraction quality of single-crystal data of some MOF crystals at room temperature is better than that at 100 K. They also proposed that the interactions between disordered solvent guest molecules and framework dominate the crystallographic diffraction quality (Lee et al., 2018). Considering the extreme importance of single-crystal diffraction technology in modern chemical structure analysis, it is of great significance to further study such phenomenon and explore whether there are other influencing factors.

Flexible metal-organic frameworks (*f*-MOFs), a branch of network chemistry, have the characteristics of reversible breathing response to physical and chemical external stimuli and have broad application prospects in the fields (Freund et al., 2021; Ji et al., 2020) of drug release (Wu et al., 2018), gas storage and separation (Carrington et al., 2017), or sensors (Horike et al., 2009). So far, a large number of *f*-MOF studies have focused on pore adjustment or configuration changes triggered by several factors (Bigdeli et al., 2020; Ghoufi et al., 2017; Krause et al., 2020; Kundu et al., 2019; Liu et al., 2020; Müller et al., 2018; Pang et al., 2016; Payne et al., 2018; Sakata et al., 2013; Tanaka and Kitagawa, 2008; Vanduyfhuys et al., 2018; Yu et al., 2019; Yuan et al., 2017), which is typically recorded by *in situ* powder X-ray diffraction (Llewellyn et al., 2006, 2009). Thermodynamic factor was considered to be one of the most important factors to affect the dynamic structural changes of some *f*-MOFs (Cheetham et al., 2018; Chen et al., 2017; Han et al., 2019; Lollar et al., 2019; Nanthamathee et al., 2014; Novendra et al., 2020; Yuan et al., 2016). For example,

[1]State Key Laboratory of Fine Chemicals, Dalian University of Technology, Dalian 116024, China

[2]School of Chemical Engineering, Dalian University of Technology, Dalian 116024, China

[3]Zhang Dayu College of Chemistry, Dalian University of Technology, Dalian 116024, China

[4]Lead contact

*Correspondence: zhangjj@dlut.edu.cn (J.-J.Z.), cyduan@dlut.edu.cn (C.D.)

https://doi.org/10.1016/j.isci.2021.103398

thermodynamic variations of structural expansion have attracted increasing attention (Chen et al., 2017; Mertsoy et al., 2021; Vanduyfhuys et al., 2018) and have been used to optimize materials for guest sorption and other applications (Calvo Galve et al., 2021; Evans et al., 2016; Krause et al., 2020; Wang et al., 2019; Yang et al., 2020). Woodfield and coworkers (Rosen et al., 2020) demonstrated for the first time that ZIF-8 also undergoes structural deformation when adsorbing small-sized CO_2 molecules by measuring changes in thermodynamic data. Gu et al. (2020) demonstrated an effective structure-deformation-thermodynamic-energy-modulation strategy, which achieved the selective adsorption of guest molecules by *f*-MOF. Other studies, including the thermodynamic measurements used to study the mechanisms of adsorption (Drout et al., 2020, 2021; Kato et al., 2020) or photocatalysis (Sun et al., 2020) in MOFs, have also been investigated. However, the influence of thermodynamic factors on the diffraction quality of single crystals of *f*-MOFs has not been reported.

This article reports an abnormal crystallographic phenomenon in the single-crystal diffraction data of an *f*-MOF $(Me_2NH_2)[Zn_2(L)(H_2O)]\cdot 3DMA\cdot 3H_2O$ (**1-g**) (H_5L = 2,5-(6-(3-carboxyphenylamino)-1,3,5-triazine-2,4-diyl-diimino)diterephthalic acid) (DMA = N,N-dimethylacetamide), which is prepared according to reference with some modifications (Zhao et al., 2018). Three SCXRD diffraction datasets of one same single crystal of **1-g** were collected at 150, 200, and 291 K, respectively, and their comparison reveals that the data quality follows the sequence data (291 K) > data (200 K) > data (150 K). **1-g** also bears an anisotropic thermal expansion with a record-high *c*-axial expansion coefficient up to 1,401.8 × 10^{-6} K^{-1} that is mainly dominated by the configuration change of the dinuclear node. *In situ* variable temperature powder X-ray diffraction (VT-PXRD) study shows that the dynamic changes of the framework are reversible. Such breathing behavior is caused by the cooperation of solvent guest molecules and temperature. Calculation based on density functional theory (DFT) reveals that the framework configuration at 291 K is more thermodynamically stable and also bears lower vibrational energy than that at 150 K, which suggests that a more thermodynamically stable configuration may dominate the crystallographic diffraction quality of **1-g**. Details of the experiments and calculations are presented.

RESULTS AND DISCUSSION

Crystal diffraction analysis

1-g crystallizes in the tetragonal *I4* space group. Its framework is constructed by $\{Zn_{24}(L)_8\}$ supramolecular building block (SBB) whose structure can be described as a cavity with a diameter ~20 Å (Figures 1F and S1). The X-ray diffraction data of the as-synthesized single crystal of **1-g** were collected at 291, 200, and 150 K, respectively. Remarkably, the results show that the intensity of diffraction points (along the (hk0) direction) in the high-angle region at 291 K is significantly stronger than those at 150 K. The related highest resolution values (d_{min}) calculated at I/σ = 3 increase from 0.75 (291 K) to 0.97 (150 K) (Figure S2, Table S1). To rule out that this abnormal phenomenon is caused by the quality difference of different crystals and the different degrees of weathering when the crystal is exposed to the air for different times, successive SCXRD experiments using the same single crystal were carried out from low to room temperature. The same trend with improved diffraction data at higher temperatures is observed (Figures 1A–1C). The corresponding d_{min} values are 0.98 (150 K, initial), 0.84 (200 K), and 0.75 Å (291 K, final), respectively (Table S2). Mosaicity, an index that depicts the misalignment of the domains in the crystal (Guionneau et al., 2012), was measured during the whole data collection process, and the corresponding values are 0.41 (150 K), 0.40 (200 K), and 0.39 (291 K), respectively (Table 1). The decrease in mosaicity is also consistent with the abnormal diffraction phenomenon.

Wilson plot, a statistical protocol to analyze the average attenuation of X-ray scattering by thermal motion, is adopted here to quantify the quality of collected diffraction datasets (Figure 1D) (YÜ, 1942). The fitted linear slope is *-2B*, where *B* (temperature factor) is proportional to the mean displacement of the atoms in the unit cell (Sun et al., 2019). A smaller *B* is preferable due to smaller thermal motion of the atoms allowing a more precise structure. The integrated data show that the *B* factor shows an overall downward trend with increasing temperature, and its value drops from 5.425 (150 K) to 3.32 (291 K) $Å^2$ (Table 1). The total diffraction intensity ($\Sigma I_{(hkl)}$) also increases with temperature.

In situ VT-PXRD experiment of **1-g** was also carried out from 150 to 650 K. The results show that the diffraction intensity of the peak at 8.72° (2θ), corresponding to the (211) and (310) crystal planes, gradually increases as the temperature increases from 150 to 290 K and at the same time the peak shape becomes narrower. Similar phenomena were also observed for high-angle diffraction peaks that correspond to the

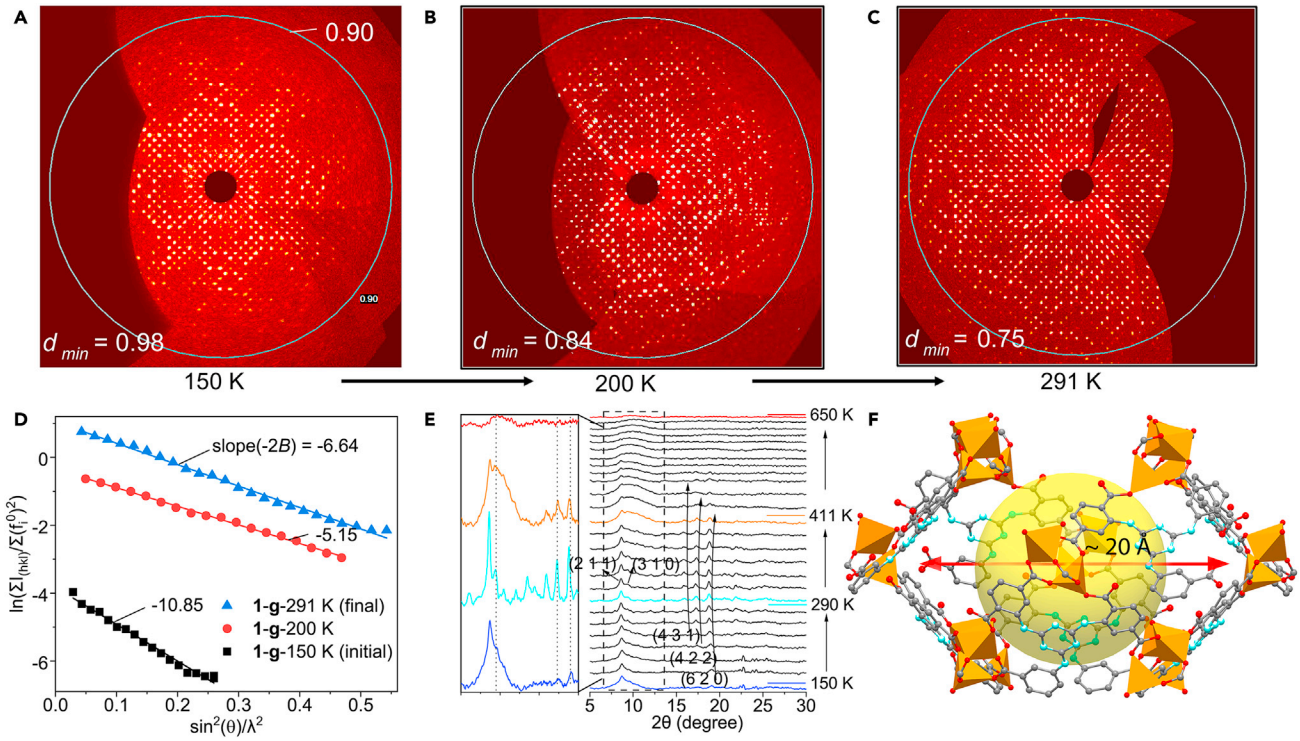

Figure 1. Temperature-dependent diffraction investigation of as-synthesized crystal of 1-g

(A–C) Synthesized process images of (hk0) of the data collected at (A) 150 K (initial), (B) 200 K (medial), and (C) 291 K (final). The highest reflection resolution d_{min} is appended at the lower left, and d = 0.90 Å as a reference is marked with a circle.

(D) Wilson plots of the data collected at 150 K (initial), 200 K (medial), and 291 K (final).

(E) VT-PXRD patterns for **1-g** as the temperature increases from 150 to 650 K.

(F) The structure of the $\{Zn_{24}(L)_8\}$ SBB. The cavity is represented as a yellow ball. Color code: gray, C; red, O; azure, N; gold polyhedral, Zn.

(620), (422), and (431) crystal planes (Figures 1E and S3). These observations indicate that the crystallinity of **1-g** increases as the temperature increases from 150 K to 290 K, which is consistent with the observed single-crystal diffraction results. When the temperature further increases, the diffraction peak of **1-g** decreases until it transforms into an amorphous phase at 650 K. In addition, the final single-crystal structure refinement results show that when the temperature increases, the Zn atomic displacement parameter (ADP) decreases from 0.08185 (150 K) to 0.04487 (291 K) $Å^2$ (Table 1), indicating a lower positional disorder at a higher temperature for **1-g**.

Breathing behavior of 1-g

The refined unit cells of the three datasets of **1-g** collected at 150, 200, and 291 K present an anisotropic thermal expansion. The *a* (and *b*) axis decreases from 30.530 (150 K) to 29.8612 (200 K) to 29.590 (291 K) Å, and the corresponding thermal expansion coefficients are -438.1×10^{-6} (150–200 K) and -218.4×10^{-6} K^{-1} (150–291 K), respectively. Similar phenomena were also observed in literature reports (Henke et al., 2013; Zhuo et al., 2020). In contrast, the length of the *c* axis increases from 14.607 (150 K) to 15.6308 (200 K) to 16.196 Å (291 K) with expansion coefficients of $1{,}401.8 \times 10^{-6}$ (150–200 K) and 771.5×10^{-6} K^{-1} (150–291 K), respectively (Table 1). The positive expansion coefficient of the *c* axis ($1{,}401.8 \times 10^{-6}$ K^{-1}) greatly exceeds the reported records of 653.2×10^{-6} K^{-1} for MOFs (Pang et al., 2016) and $1{,}200 \times 10^{-6}$ K^{-1} for polymers (Shen et al., 2013). Totally, as the temperature rises, the unit cell volume increases by about 4.0%, and the corresponding solvent-accessible volume has the same increasing trend (Table S3, Figure S4).

Such an anisotropic thermal expansion behavior is usually related to changes in the framework configurations (Burtch et al., 2019; Henke et al., 2013; Pang et al., 2016; Yeung et al., 2016). Therefore, we first investigated the configuration changes of the ligands in the framework during the temperature change process. The refined crystal structure of **1-g** shows that there are strong intraligand N-H···O hydrogen bonds

Table 1. Temperature-dependent structure parameters and diffraction data quality of 1-g

temp (K)	B (Å^2)	Zn atomic displacement parameters (Å^2)	Dimensions (Å)	Expansion coefficients ($\times 10^{-6}$ K^{-1})	Void (Å^3)	Unit cell (Å^3)	Resolution (Å) at $< I/\sigma > = 3$	mosa. (deg)
150	5.43	0.08185(5)	a = 30.530(3) c = 14.607(3)	0 0	9,421.7 (69.2%)	13,615.0	0.98	0.41
200	2.57	0.033215(10)	a = 29.8612(8) c = 15.6308(7)	α_a = −438.1 α_c = 1,401.8	9,759.0 (70.0%)	13,937.9	0.84	0.40
291	3.32	0.04487(10)	a = 29.590(6) c = 16.196(5)	α_a = −218.4 α_c = 771.5	10,160.9 (71.7%)	14,181.0	0.75	0.39

(Figure S5), in which the secondary amino group (-NH) acts as H-donor and the adjacent carboxylate oxygen as H-acceptor. As the temperature changes, the bond length and bond angle hover in the ranges of 2.58–2.61 Å and 130.8° ∼ 134.1°, respectively (Table S5). However, the change in the configuration of the ligand is still relatively small compared with those reported in the literature (Garai et al., 2020; Pang et al., 2016). Therefore, the configuration distortion of the ligand in the framework during the temperature change process cannot be the main reason for the large thermal expansion coefficient.

Furthermore, the influence of the configuration change of the metal node on the thermal expansion behavior of the compound during the temperature change process was studied. The binuclear quasi-paddle-wheel unit {$Zn_2(L)_3$} (Figure 2), constituted by two zinc ions and three deprotonated ligands, is selected as an analysis model. The unit has three bridged carboxylate groups (COO1, COO2, and COO3) and two axial mono-coordinated carboxylate groups (Figure 2A). The two coordination angles, C22-O9-Zn2 and C22-O10-Zn1 formed by the coordination of COO1 and Zn^{2+} ions along the *c* direction, both increase with increasing temperature. The former increases from 123.7° to 132.0°, whereas the latter increases from 132.5° to 134.0°. Also, the related torsion angle of Zn1-C26-O9-Zn2 decreases from 51.1° to 25.6°. In contrast, both COO2 and COO3 groups bear a one-way swing, resulting in an opposite variation of the C-O-Zn bond angle in each carboxylic group with increasing temperature. Interestingly, when temperature increases to 291 K, the bond angles related to the COO2 group (∠C24-O5-Zn1 [150.3°] and C24-O6-Zn2 [119.7°]) are almost the same as those of the COO3 group (∠C22-O2-Zn2 [150.6°] and ∠C22-O1-Zn1 [119.6°]) (Figures 2A–2D). This symmetrical evolution of the framework may help reduce the structural energy (Gong et al., 2016). More importantly, with the changes in the bond angles and torsion angles related to the carboxylate group, the two key angles (∠O1-Zn1-O5 and ∠O6-Zn2-O9) that determine the opening of the binuclear unit have also changed accordingly. ∠O1-Zn1-O5 decreases from 109.2° (150 K) to 105.6° (291 K), whereas ∠O6-Zn2-O9 increases from 93.6° (150 K) to 108.9° (291 K). This change in the coordination angles promotes the expansion of the "wheel paddle" in the {$Zn_2(L)_3$} unit from 94.7° (150 K) to 113.4° (291 K), which further leads to a size increase from 23.17 Å (150 K) to 24.50 Å (291 K) of the {$Zn_{24}(L)_8$} SBB along the *c* direction (Figure 2F). The aforementioned results reveal that the structural expansion behavior of the compound with increasing temperature is mainly dominated by the configuration change of the inorganic node. Similar results have also been reported by Kitagawa and coworkers (Matsuda et al., 2004).

In situ VT-PXRD experiments of **1-g** from 290 K to 150 K, and then from 150 K to 290 K, were carried out to study the dynamic changes of the framework during the temperature cycle process (Figure 3). The results show that when the temperature drops from 290 K to 150 K, the diffraction peaks of (211) and (620) gradually shift to a higher angle, and the maximum displacement values are 0.16° and 0.30° for the two peaks, respectively. When the temperature returns from 150 K to 290 K, the diffraction peaks gradually return to the initial positions. Such results indicate that the interplanar spacing of (211) and (620) plane changes reversibly according to Bragg's law ($2d\sin\theta = n\lambda$), which means that the crystal of **1-g** bears a reversible expansion/contraction during the cycle. Second, the diffraction peaks of (211), (431), and (620) are relatively sharp at the initial temperature (290 K) and gradually passivated as the temperature drops to 150 K, and then the peaks recover when the temperature rises to 290 K. The aforementioned results further prove that the crystallinity of crystal **1-g** gradually increases with increasing temperature, and this phenomenon is reversible.

Breathing behavior induced by the solvent guest molecules and temperature

The solvent guest molecule in the framework is generally considered to be one of the important factors affecting the breathing behavior of the framework (Carrington et al., 2017; Dybtsev et al., 2004). Therefore,

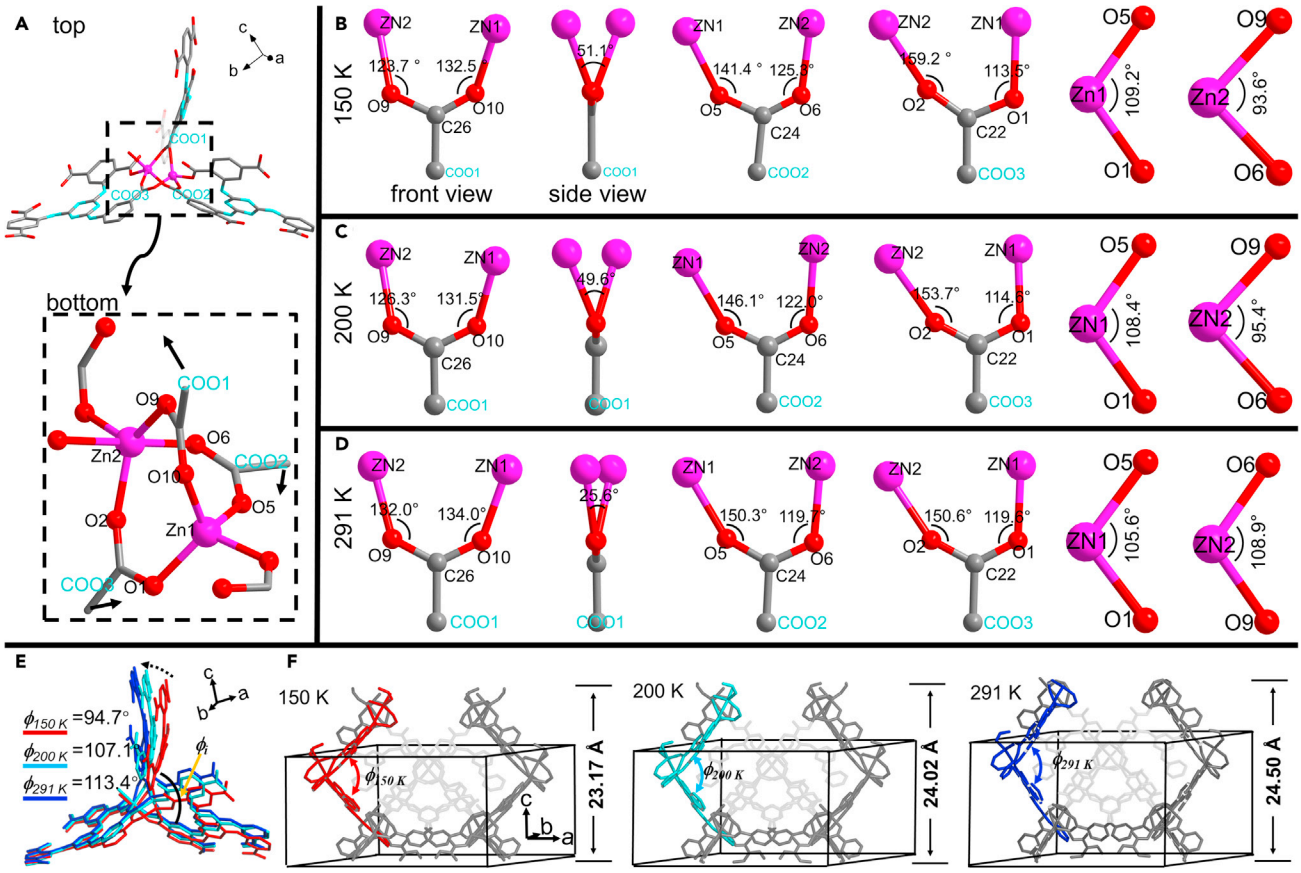

Figure 2. Detailed configuration changes of the 1-g at different temperatures

(A) The refined configuration of binuclear unit $\{Zn_2(L)_3\}$ (top) and the coordination detail of the binuclear unit (bottom).

(B–D) The changes of bond angle and torsion angle of the binuclear cluster as the temperature rises from 150 (B), 200 (C), and 291 K (D).

(E) The changes of binuclear $\{Zn_2(L)_3\}$ unit as the temperature increases.

(F) Corresponding cavity sizes ($\{Zn_{24}(L)_8\}$) of **1-g** at different temperatures (the rectangular box represents the unit cell).

a new phase (**1-e**) with some solvent molecules removed was obtained by heating **1-g** under vacuum at 353 K and was used to study the crystallographic behavior of solvent loss crystal. Thermogravimetric analysis (TGA) and differential scanning calorimetry results show that solvent molecules in **1-e** still account for ~19% of the weight (Figures S6 and S7). Therefore the formula of **1-e** is **1**•2DMA•2H_2O, as also confirmed by elemental analysis.

Single-crystal diffraction results show that the diffraction ability of **1-e** at 150 K and 291 K is almost the same, and the highest diffraction angles (2θ) are 11.88° and 12.09° for the data collected at the two temperatures, respectively. Unfortunately, due to the serious lack of collected data, it is impossible to refine the precise structure and related lattice parameters of **1-e**. *In situ* VT-PXRD method is also employed to check the dynamic changes of the framework of **1-e** during a temperature cycle process of 151 K → 301 K → 151 K. The results show that the diffraction peak of **1-e** does not change significantly with the change of temperature (Figures S8 and S9). By comparing the *in situ* VT-PXRD results of **1-e** and **1-g**, it can be determined that when the content of guest solvent molecules in **1-g** exceeds a certain critical value, the solvent molecules become the key factor in inducing the breathing behavior of the framework. Temperature is a stimulus factor for this behavior. A similar result has also been reported by Kundu et al. (2019).

Furthermore, the effect of surface tension of solvent on such breathing response is also considered (Kundu et al., 2019). First, four mixed solvents of DMA + H_2O with different surface tensions (38.21, 40.98, 42.95, and 46.76 mN/m) were prepared by adjusting the ratio of the two solvents. Second, four crystals were prepared using the same H_5L and $Zn(NO_3)_2$ $6H_2O$ raw materials as that of **1-g**, but the aforementioned four mixed

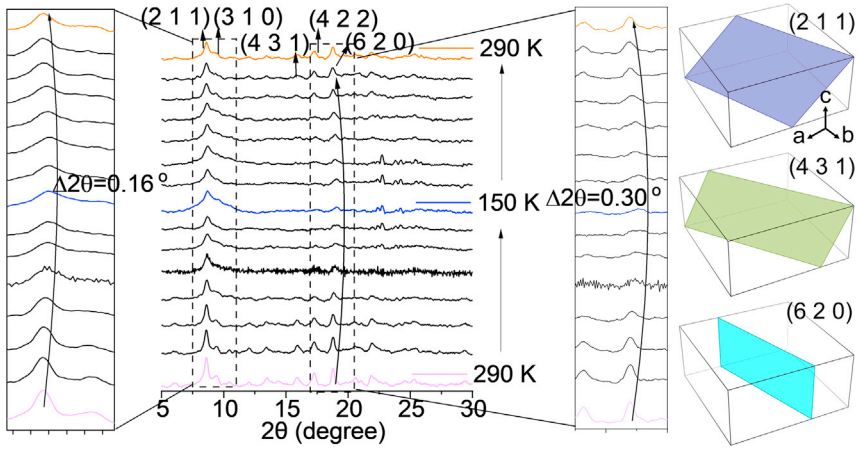

Figure 3. *In situ* VT-PXRD patterns for 1-g as the temperature swings from 290 to 150 then back to 290 K (left) and the crystal plane in the unit cell (right).

solvents were used as the synthesis solvents, respectively. TGA results of the four samples show that the DMA:H_2O ratio of the guest solvents of the samples is different, which means that they have different tensions (Figure S10A). The SCXRD data of the four crystals were collected at 150 and 291 K, respectively. However, the results show that the diffraction data quality and lattice parameters of the four crystals are almost undifferentiated at the same temperature (Tables S6 and S7). Interestingly, when these mixed solvents with different surface tensions were frozen to the liquid nitrogen temperature, they have similar gross shrinkage (Figure S10B). Therefore, the change of surface tension of the captured solvent molecules has little effect on the breathing behavior of the framework.

Mechanisms dominating the inverse crystallographic diffraction

Disordered interactions in f-MOF

When studying the factors that affect the quality of crystal diffraction, Yaghi et al. (Lee et al., 2018) suggested that the reduction of the interaction between the guest and the host can reduce the vibration of the framework, thereby increasing the diffraction intensity. Therefore, the influence of the host-guest interaction on the diffraction of the crystal in this paper was studied.

Such interactions can be evaluated by comparing the intensity of the residual electron clouds (RECs) associated with the guest solvent molecules at different temperatures. Disordered guest molecules in the cavity of MOFs often produce irregular diffraction of X-rays, which appear as a large number of RECs after resolving the frameworks of MOFs. These RECs cannot be used to figure out the precise structure of the solvent in the cavity, and PLATON software (Spek, 2008b) is typically used to calculate and remove these electrons (Spek, 2015). However, for the same crystal, the visualization of the residual electron density of the data collected at different temperatures can directly reflect the degree of temperature-dependent disorder of the guests in the cavity (He et al., 2017; Takashima et al., 2014). Generally, the weaker the RECs, the more disordered the guest molecules inside the framework (Lee et al., 2018; Ryland, 1958).

A detailed comparison of the data of **1-g** collected at different temperatures shows that the visualized Fourier-synthesized 3D electron density (F_O - F_C) of the guests in the unit cell presents a sparser local residual electronic density with increasing temperature (Figures 4A–4C). For example, the high residual electronic density (red region) in the unit cell in the data collected at 150 K is hardly observed in the 291 K data, and a large amount of low residual electron density (green area) also disappears. Besides, the electron counts in the unit are found to be 1,591 (150 K), 1,655 (200 K), and 1,463 (291 K), respectively. These observations indicate that the guest molecules become more disordered at higher temperatures, resulting in lower solvent strain interacting with the framework, which may promote stronger diffraction intensity at a high angle. A similar phenomenon has also been observed in the literature (Lee et al., 2018). However, the aforementioned experimental results show that the surface-tension-dependent changes in lattice and diffraction resolution of **1-g** are negligible (Tables S6 and S7), suggesting that the disordered host-guest interactions may not be the key factor to control the quality of the crystal diffraction.

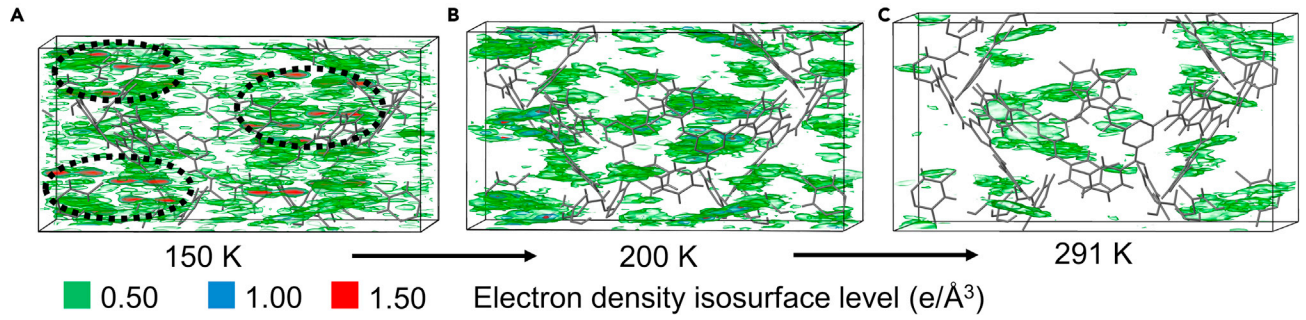

Figure 4. Fourier-synthesized 3D electron density (F_O - F_C) in the pores of 1-g at different temperatures

(A–C) The 3D electron density maps of the guest molecules in the unit cell of **1-g** at 150 (A), 200 (B), and 291 K (C), respectively. The levels of the electron density (F_O - F_C) are marked by red, blue, and green isosurfaces. The framework in the unit cell is shown here to facilitate the evaluation of the relative position of the electron density.

Thermodynamically stable configuration in 1-g induced by thermal-solvent cooperatively

The breathing behavior of **1-g** inspired us to further speculate that temperature and solvent probably may co-induce a more thermodynamically stable configuration at room temperature, leading to a reduction in framework vibration, thereby enhancing the quality of crystal diffraction. That is to say, the contracted framework of **1-g** at cryogenic temperature possesses higher thermodynamic energy, thereby decreasing the intensity of Bragg reflections. On the contrary, the expansive framework at higher temperatures can have lower thermal vibrations, resulting in a more thermodynamically stable configuration.

We carried out theoretical studies on **1-g**'s three configurations **1-g-150** (150 K), **1-g-200** (200 K), and **1-g-291** (291 K) induced by the breathing behavior. Geometry optimization and internal energy calculation were performed using the periodic density functional theory (PDFT) method through the DMol3 module in the Material Studio software package (Tables S8 and S9) (Delley, 1990, 2000). The calculated results show that the optimized values of φ of models **1-g-150**, **1-g-200,** and **1-g-291** are 86.8°, 102.4°, and 110.6°, respectively. Interestingly, of the three configurations, **1-g-150** has the highest relative energy, whereas **1-g-291** has the lowest. Similar unit cell volume-dependent energy change has also been observed in the literature (Coudert et al., 2008; Iacomi et al., 2021). The energy difference of unit cell between **1-g-150** and **1-g-200** (ΔE_1) is 1.71 kcal/mol, and the ΔE_2 between **1-g-200** and **1-g-291** is 0.61 kcal/mol (Figure 5A). That is, among the above three configurations, **1-g-291** is the most thermodynamically stable one, followed by **1-g-200**, and finally **1-g-150**. This sequence is positively correlated with the corresponding temperature-dependent diffraction quality of the crystal.

Then the thermodynamic vibration energy of the three configurations was evaluated. The $\{Zn_2(L)_3\}$ binuclear unit, which could represent the configuration characteristics of the framework, was truncated from each optimized framework, and the corresponding models were named as **$\{Zn_2(L)_3\}$-150** (150 K), **$\{Zn_2(L)_3\}$-200** (200 K), and **$\{Zn_2(L)_3\}$-291** (291 K), respectively. The vibrational frequency of each model was calculated using the DFT method, and the results are listed in Table S10. The contribution of three kinds of relative kinetic energies including translational, rotational, and vibration energy is shown in the radar chart of Figure 5B. The results show that the translational and rotational energies of the three models are the same ($\Delta E_t = 0$, $\Delta E_r = 0$), but their vibrational energies are different. Taking the vibrational energy of **$\{Zn_2(L)_3\}$-291** as a reference, **$\{Zn_2(L)_3\}$-150** presents the maximum relative vibration energy (ΔE_{v1} = 0.57 kcal/mol), followed by **$\{Zn_2(L)_3\}$-200** (ΔE_{v2} = 0.37 kcal/mol). This sequence is also consistent with that of the configuration-dependent energy.

Therefore, these results suggest that the framework of **1-g** gradually transfers to a more thermodynamically stable configuration as the temperature increases, and the thermodynamically vibrational energy of the framework decreases, reducing the disorder of the framework, thus promoting the crystallographic diffraction quality of **1-g**.

On the basis of the aforementioned observations, it is clear that a high crystallographic diffraction quality probably can be induced not only by a lower test temperature but also by a more thermodynamically stable

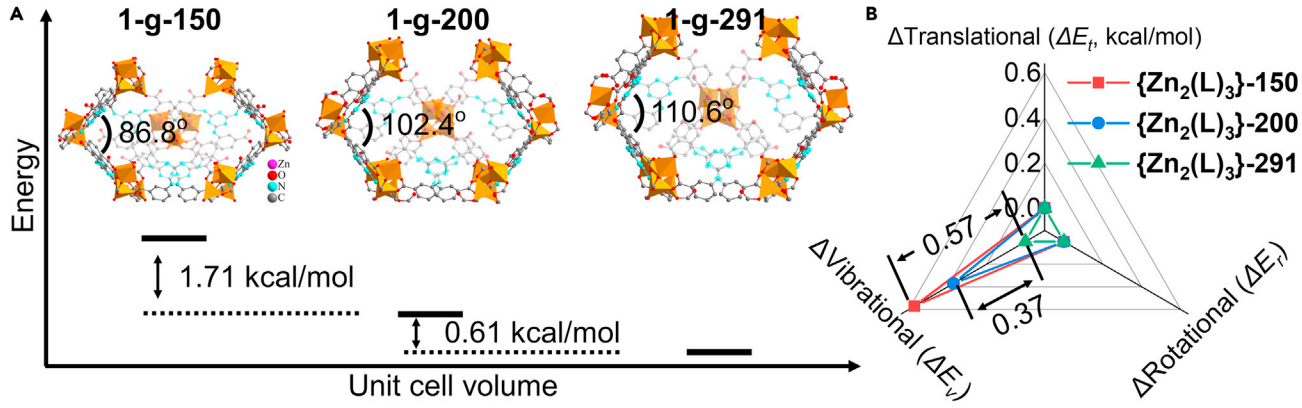

Figure 5. The configuration-dependent relative energy of 1-g

(A) The relative energy of the configurations **1-g-150**, **1-g-200,** and **1-g-291**.

(B) The radar chart of relative translational, rotational, and vibrational energies of the binuclear unit **{$Zn_2(L)_3$}-150**, **{$Zn_2(L)_3$}-200,** and **{$Zn_2(L)_3$}-291**.

configuration of the framework or the decreased disordered guest-host interaction. Whether it is better to collect the single-crystal diffraction data at low or room temperatures depends on the factor that plays the dominating role among the three of them. This work suggests that for crystals with poor crystallographic diffraction at low temperature, one can try to adjust the test temperature to see whether a more thermodynamically stable configuration can be induced, thereby improving diffraction quality and structural resolution.

Conclusions

In summary, this work shows an abnormal crystallography in the *f*-MOF of **1-g**, that is, the diffraction quality of the single crystal at cryogenic temperature is lower than that collected at a higher temperature. Framework **1-g** presents a reversible breathing behavior accompanied by an anisotropic thermal expansion behavior with a record-high *c-axial* positive expansion coefficient of 1,401.8 × 10^{-6} K^{-1}, which is induced by thermal and guest-solvent cooperatively. Disordered solvent-framework interaction is not considered to be the main factor in affecting the abnormal crystallography. Calculation results suggest that the thermodynamic energy of the framework configuration decreases with the increase of temperature, indicating that the thermodynamics of the configuration is more stable at a higher temperature. Such a stable configuration also exhibits a lower vibrational frequency, thereby reducing the disorder of crystallography and improving diffraction quality. This work not only enriches the fundamental research of crystallography but also provides a new clue on how to improve the test data quality of X-ray single-crystal diffraction technology.

Limitations of the study

This work focuses on an interesting phenomenon that a high-quality Bragg diffraction of an *f*-MOF prefers a thermodynamically stable configuration, but it details only one MOF. Furthermore, thermodynamics of the *f*-MOF was considered to affect its crystallographic diffraction behavior, but the kinetics, including the changes of guest solvent when temperature increases, should be considered in future studies.

STAR★METHODS

Detailed methods are provided in the online version of this paper and include the following:

- KEY RESOURCES TABLE
- RESOURCE AVAILABILITY
  - Lead contact
  - Materials availability
  - Data and code availability
- METHOD DETAILS
  - General
  - Synthesis of ligand (H_5L)

- Synthesis of $(Me_2NH_2)[Zn_2(L)(H_2O)]\cdot 3DMA\cdot 3H_2O$ (1-g)
- Synthesis of MOFs in the solvent with various surface tension
- Synthesis of 1-e
- The surface tension measurement
- Single crystal X-ray crystallography
- Computational details

SUPPLEMENTAL INFORMATION

Supplemental information can be found online at https://doi.org/10.1016/j.isci.2021.103398.

ACKNOWLEDGMENTS

This work was supported by the National Natural Science Foundation of China (grant No. 21871038). We thank the platform of the Chemical Engineering Testing Center and Yu-Zhen Pan from the Dalian University of Technology for basic equipment support. We thank Yu-Jie Yin from our laboratory for photo collection. We gratefully appreciate the Network and Information Center of Dalian University of Technology for computational resources. We also acknowledge Dong-Dong Wang from the Dalian Institute of Chemical Physics, Chinese Academy of Sciences, for her technical support with various temperature powder X-ray diffraction experiments.

AUTHOR CONTRIBUTIONS

Conceptualization, H.Z. and J.-J.Z.; methodology, H.Z.; investigation, H.Z., J.H., P.-P.Z, W.-J.F., S.L., X.-D.S.; writing – original draft, H.Z.; writing – review & editing, H.Z. and J.-J.Z.; funding acquisition, J.-J.Z.; resources, J.-J.Z.; supervision, J.-J.Z. and C.D.

DECLARATION OF INTERESTS

The authors declare no competing interests.

Received: August 23, 2021
Revised: October 6, 2021
Accepted: October 29, 2021
Published: December 17, 2021

REFERENCES

Bigdeli, F., Lollar, C.T., Morsali, A., and Zhou, H.-C. (2020). Switching in metal–organic frameworks. Angew. Chem. Int. Ed. *59*, 4652–4669. https://doi.org/10.1002/anie.201900666.

Bragg, W.L., and Bragg, W.H. (1913). The structure of some crystals as indicated by their diffraction of X-rays. Proc. R. Soci. Lond. Ser. A. Contain. Pap. A Math. Phys. *89*, 248–277. https://doi.org/10.1098/rspa.1913.0083.

Burtch, N.C., Baxter, S.J., Heinen, J., Bird, A., Schneemann, A., Dubbeldam, D., and Wilkinson, A.P. (2019). Negative thermal expansion design strategies in a diverse series of metal–organic frameworks. Adv. Funct. Mater. *29*, 1904669. https://doi.org/10.1002/adfm.201904669.

Calvo Galve, N., Abrishamkar, A., Sorrenti, A., Di Rienzo, L., Satta, M., D'Abramo, M., Coronado, E., de Mello, A.J., Mínguez Espallargas, G., and Puigmartí-Luis, J. (2021). Exploiting reaction-diffusion conditions to trigger pathway complexity in the growth of a MOF. Angew. Chem. Int. Ed. *60*, 15920–15927. https://doi.org/10.1002/anie.202101611.

Carrington, E.J., McAnally, C.A., Fletcher, A.J., Thompson, S.P., Warren, M., and Brammer, L. (2017). Solvent-switchable continuous-breathing behaviour in a diamondoid metal-organic framework and its influence on CO2 versus CH4 selectivity. Nat. Chem. *9*, 882–889. https://doi.org/10.1038/nchem.2747.

Cheetham, A.K., Kieslich, G., and Yeung, H.H.M. (2018). Thermodynamic and kinetic effects in the crystallization of metal–organic frameworks. Acc. Chem. Res. *51*, 659–667. https://doi.org/10.1021/acs.accounts.7b00497.

Chen, Q., Feng, R., Xu, J., Jia, Y.-Y., Wang, T.-T., Chang, Z., and Bu, X.-H. (2017). Kinetic and thermodynamic control of structure transformations in a family of cobalt(II)–organic frameworks. ACS Appl. Mater. Inter. *9*, 35141–35149. https://doi.org/10.1021/acsami.7b12925.

Coudert, F.-X., Jeffroy, M., Fuchs, A.H., Boutin, A., and Mellot-Draznieks, C. (2008). Thermodynamics of guest-induced structural transitions in hybrid organic–inorganic frameworks. J. Am. Chem. Soc. *130*, 14294–14302. https://doi.org/10.1021/ja805129c.

Delley, B. (1990). An all-electron numerical method for solving the local density functional for polyatomic molecules. J. Chem. Phys. *92*, 508–517. https://doi.org/10.1063/1.458452.

Delley, B. (2000). From molecules to solids with the DMol3 approach. J. Chem. Phys. *113*, 7756–7764. https://doi.org/10.1063/1.1316015.

Deng, H., Grunder, S., Cordova, K.E., Valente, C., Furukawa, H., Hmadeh, M., Gándara, F., Whalley, A.C., Liu, Z., Asahina, S., et al. (2012). Large-pore apertures in a series of metal-organic frameworks. Science *336*, 1018. https://doi.org/10.1126/science.1220131.

Drout, R.J., Kato, S., Chen, H., Son, F.A., Otake, K.-i., Islamoglu, T., Snurr, R.Q., and Farha, O.K. (2020). Isothermal titration calorimetry to explore the parameter space of organophosphorus agrochemical adsorption in MOFs. J. Am. Chem. Soc. *142*, 12357–12366. https://doi.org/10.1021/jacs.0c04668.

Drout, R.J., Gaidimas, M.A., and Farha, O.K. (2021). Thermochemical investigation of oxyanion coordination in a Zirconium-Based metal–organic framework. ACS Appl. Mater. Inter. https://doi.org/10.1021/acsami.1c05271.

Dybtsev, D.N., Chun, H., and Kim, K. (2004). Rigid and flexible: a highly porous metal–organic framework with unusual guest-dependent dynamic behavior. Angew. Chem. Int. Ed. *43*,

5033–5036. https://doi.org/10.1002/anie.200460712.

Evans, J.D., Bocquet, L., and Coudert, F.-X. (2016). Origins of negative gas adsorption. Chem *1*, 873–886. https://doi.org/10.1016/j.chempr.2016.11.004.

Freund, R., Zaremba, O., Arnauts, G., Ameloot, R., Skorupskii, G., Dincă, M., Bavykina, A., Gascon, J., Ejsmont, A., Gościańska, J., et al. (2021). The current status of MOF and COF applications. Angew. Chem. Int. Ed. https://doi.org/10.1002/anie.202106259.

Frisch, M.J., Trucks, G.W., Schlegel, H.B., Scuseria, G.E., Robb, M.A., Cheeseman, J.R., Scalmani, G., Barone, V., Mennucci, B., Petersson, G.A., et al. (2016). Gaussian 16, Revision A.03 (Gaussian Inc.).

Garai, B., Bon, V., Efimova, A., Gerlach, M., Senkovska, I., and Kaskel, S. (2020). Reversible switching between positive and negative thermal expansion in a metal–organic framework DUT-49. J. Mater. Chem. A *8*, 20420–20428. https://doi.org/10.1039/D0TA06830F.

Ghoufi, A., Benhamed, K., Boukli-Hacene, L., and Maurin, G. (2017). Electrically induced breathing of the MIL-53(Cr) metal–organic framework. ACS Cent. Sci. *3*, 394–398. https://doi.org/10.1021/acscentsci.6b00392.

Goeta, A.E., and Howard, J.A.K. (2004). Low temperature single crystal X-ray diffraction: advantages, instrumentation and applications. Chem. Soc. Rev. *33*, 490–500. https://doi.org/10.1039/B312763J.

Gong, J.Q., Favereau, L., Anderson, H.L., and Herz, L.M. (2016). Breaking the symmetry in molecular nanorings. J. Phys. Chem. Lett. *7*, 332–338. https://doi.org/10.1021/acs.jpclett.5b02617.

Grimme, S., Antony, J., Ehrlich, S., and Krieg, H. (2010). A consistent and accurate ab initio parametrization of density functional dispersion correction (DFT-D) for the 94 elements H-Pu. J. Chem. Phys. *132*, 154104. https://doi.org/10.1063/1.3382344.

Gu, Y., Zheng, J.J., Otake, K.I., Sugimoto, K., Hosono, N., Sakaki, S., Li, F., and Kitagawa, S. (2020). Structural-deformation-energy-modulation strategy in a soft porous coordination polymer with an interpenetrated framework. Angew. Chem. Int. Ed. Engl. *59*, 15517–15521. https://doi.org/10.1002/anie.202003186.

Guionneau, P., Lakhloufi, S., Lemée-Cailleau, M.-H., Chastanet, G., Rosa, P., Mauriac, C., and Létard, J.-F. (2012). Mosaicity and structural fatigability of a gradual spin-crossover single crystal. Chem. Phys. Lett. *542*, 52–55. https://doi.org/10.1016/j.cplett.2012.06.005.

Günther, S., Reinke, P.Y.A., Fernández-García, Y., Lieske, J., Lane, T.J., Ginn, H.M., Koua, F.H.M., Ehrt, C., Ewert, W., Oberthuer, D., et al. (2021). X-ray screening identifies active site and allosteric inhibitors of SARS-CoV-2 main protease. Science *372*, 642–646. https://doi.org/10.1126/science.abf7945.

Han, Y., Sinnwell, M.A., Teat, S.J., Sushko, M.L., Bowden, M.E., Miller, Q.R.S., Schaef, H.T., Liu, L., Nie, Z., Liu, J., and Thallapally, P.K. (2019). Desulfurization efficiency preserved in a heterometallic MOF: synthesis and thermodynamically controlled phase transition. Adv. Sci. *6*, 1802056. https://doi.org/10.1002/advs.201802056.

Hay, P.J., and Wadt, W.R. (1985). Ab initio effective core potentials for molecular calculations. Potentials for K to Au including the outermost core orbitals. J. Chem. Phys. *82*, 299–310. https://doi.org/10.1063/1.448975.

He, H., Ma, E., Yu, J., Cui, Y., Lin, Y., Yang, Y., Chen, X., Chen, B., and Qian, G. (2017). Periodically aligned dye molecules integrated in a single MOF microcrystal exhibit single-mode linearly polarized lasing. Adv. Opt. Mater. *5*, 1601040. https://doi.org/10.1002/adom.201601040.

Henke, S., Schneemann, A., and Fischer, R.A. (2013). Massive anisotropic thermal expansion and thermo-responsive breathing in metal-organic frameworks modulated by linker functionalization. Adv. Funct. Mater. *23*, 5990–5996. https://doi.org/10.1002/adfm.201301256.

Horike, S., Shimomura, S., and Kitagawa, S. (2009). Soft porous crystals. Nat. Chem. *1*, 695–704. https://doi.org/10.1038/nchem.444.

Howard, J.A.K., and Probert, M.R. (2014). Cutting-edge techniques used for the structural investigation of single crystals. Science *343*, 1098–1102. https://doi.org/10.1126/science.1247252.

Huang, Z., Grape, E.S., Li, J., Inge, A.K., and Zou, X. (2021). 3D electron diffraction as an important technique for structure elucidation of metal-organic frameworks and covalent organic frameworks. Coord. Chem. Rev. *427*, 213583. https://doi.org/10.1016/j.ccr.2020.213583.

Iacomi, P., Lee, J.S., Vanduyfhuys, L., Cho, K.H., Fertey, P., Wieme, J., Granier, D., Maurin, G., Van Speybroeck, V., Chang, J.-S., and Yot, P.G. (2021). Crystals springing into action: metal–organic framework CUK-1 as a pressure-driven molecular spring. Chem. Sci. *12*, 5682–5687. https://doi.org/10.1039/D1SC00205H.

Ji, Z., Wang, H., Canossa, S., Wuttke, S., and Yaghi, O.M. (2020). Pore chemistry of metal–organic frameworks. Adv. Funct. Mater. *30*, 2000238. https://doi.org/10.1002/adfm.202000238.

Kato, S., Drout, R.J., and Farha, O.K. (2020). Isothermal titration calorimetry to investigate uremic toxins adsorbing onto metal-organic frameworks. Cell Rep. Phys. Sci. *1*, 100006. https://doi.org/10.1016/j.xcrp.2019.100006.

Krause, S., Hosono, N., and Kitagawa, S. (2020). Chemistry of soft porous crystals: structural dynamics and gas adsorption properties. Angew. Chem. Int. Ed. Engl. *59*, 15325–15341. https://doi.org/10.1002/anie.202004535.

Kundu, T., Wahiduzzaman, M., Shah, B.B., Maurin, G., and Zhao, D. (2019). Solvent-induced control over breathing behavior in flexible metal-organic frameworks for natural-gas delivery. Angew. Chem. Int. Ed. Engl. *58*, 8073–8077. https://doi.org/10.1002/anie.201902738.

Lee, R., Howard, J.A.K., Probert, M.R., and Steed, J.W. (2014). Structure of organic solids at low temperature and high pressure. Chem. Soc. Rev. *43*, 4300–4311. https://doi.org/10.1039/C4CS00046C.

Lee, S., Bürgi, H.-B., Alshmimri, S.A., and Yaghi, O.M. (2018). Impact of disordered guest–framework interactions on the crystallography of metal–organic frameworks. J. Am. Chem. Soc. *140*, 8958–8964. https://doi.org/10.1021/jacs.8b05271.

Liu, Y.T., Yin, X., Lai, X.Y., and Wang, X. (2018). Theoretical study on photophysical properties of three high water solubility polypyridyl complexes for two-photon photodynamic therapy. Phys. Chem. Chem. Phys. *20*, 18074–18081. https://doi.org/10.1039/c8cp01069b.

Liu, Z., Zhang, L., and Sun, D. (2020). Stimuli-responsive structural changes in metal-organic frameworks. Chem. Commun. (Camb) *56*, 9416–9432. https://doi.org/10.1039/d0cc03197f.

Llewellyn, P.L., Bourrelly, S., Serre, C., Filinchuk, Y., and Férey, G. (2006). How hydration drastically improves adsorption selectivity for CO2 over CH4 in the flexible chromium terephthalate MIL-53. Angew. Chem. Int. Ed. *45*, 7751–7754. https://doi.org/10.1002/anie.200602278.

Llewellyn, P.L., Horcajada, P., Maurin, G., Devic, T., Rosenbach, N., Bourrelly, S., Serre, C., Vincent, D., Loera-Serna, S., Filinchuk, Y., and Férey, G. (2009). Complex adsorption of short linear alkanes in the flexible metal-organic-framework MIL-53(Fe). J. Am. Chem. Soc. *131*, 13002–13008. https://doi.org/10.1021/ja902740r.

Lollar, C.T., Pang, J., Qin, J.-s., Yuan, S., Powell, J.A., and Zhou, H.-C. (2019). Thermodynamically controlled linker installation in flexible zirconium metal–organic frameworks. Cryst. Growth Des. *19*, 2069–2073. https://doi.org/10.1021/acs.cgd.8b01637.

Matsuda, R., Kitaura, R., Kitagawa, S., Kubota, Y., Kobayashi, T.C., Horike, S., and Takata, M. (2004). Guest shape-responsive fitting of porous coordination polymer with shrinkable framework. J. Am. Chem. Soc. *126*, 14063–14070. https://doi.org/10.1021/ja046925m.

Mertsoy, E.Y., Zhang, X., Cockreham, C.B., Goncharov, V.G., Guo, X., Wang, J., Wei, N., Sun, H., and Wu, D. (2021). Thermodynamic, thermal, and structural stability of bimetallic MIL-53 (Al1–xCrx). J. Phys. Chem. C *125*, 14039–14047. https://doi.org/10.1021/acs.jpcc.1c02623.

Momma, K., and Izumi, F. (2011). VESTA 3 for three-dimensional visualization of crystal, volumetric and morphology data. J. Appl. Crystallogr. *44*, 1272–1276. https://doi.org/10.1107/S0021889811038970.

Müller, K., Helfferich, J., Zhao, F., Verma, R., Kanj, A.B., Meded, V., Bléger, D., Wenzel, W., and Heinke, L. (2018). Switching the proton conduction in nanoporous, crystalline materials by light. Adv. Mater. *30*, 1706551. https://doi.org/10.1002/adma.201706551.

Nanthamathee, C., Ling, S., Slater, B., and Attfield, M.P. (2014). Contradistinct thermoresponsive behavior of isostructural MIL-53 type metal–organic frameworks by modifying the framework inorganic anion. Chem. Mater. *27*, 85–95. https://doi.org/10.1021/cm503311x.

Novendra, N., Marrett, J.M., Katsenis, A.D., Titi, H.M., Arhangelskis, M., Friščić, T., and Navrotsky, A. (2020). Linker substituents control the thermodynamic stability in metal–organic frameworks. J. Am. Chem. Soc. *142*, 21720–21729. https://doi.org/10.1021/jacs.0c09284.

Pang, J., Liu, C., Huang, Y., Wu, M., Jiang, F., Yuan, D., Hu, F., Su, K., Liu, G., and Hong, M. (2016). Visualizing the dynamics of temperature- and solvent-responsive soft crystals. Angew. Chem. Int. Ed. *55*, 7478–7482. https://doi.org/10.1002/anie.201603030.

Park, S.S., Hendon, C.H., Fielding, A.J., Walsh, A., O'Keeffe, M., and Dincă, M. (2017). The organic secondary building unit: strong intermolecular π interactions define topology in MIT-25, a mesoporous MOF with proton-replete channels. J. Am. Chem. Soc. *139*, 3619–3622. https://doi.org/10.1021/jacs.6b13176.

Payne, M.K., Pyrch, M.M., Jubinsky, M., Basile, M.C., and Forbes, T.Z. (2018). Impacts of oxo interactions within actinyl metal organic materials: highlight on thermal expansion behaviour. Chem. Commun. *54*, 10828–10831. https://doi.org/10.1039/c8cc05240a.

Perles, J. (2020). Characterisation and study of compounds by single crystal X-ray diffraction. Crystals *10*, 934. https://doi.org/10.3390/cryst10100934.

Renaud, J.-P., Chung, C.-w., Danielson, U.H., Egner, U., Hennig, M., Hubbard, R.E., and Nar, H. (2016). Biophysics in drug discovery: impact, challenges and opportunities. Nat. Rev. Drug Discov. *15*, 679–698. https://doi.org/10.1038/nrd.2016.123.

Rosen, P.F., Dickson, M.S., Calvin, J.J., Ross, N.L., Friščić, T., Navrotsky, A., and Woodfield, B.F. (2020). Thermodynamic evidence of structural transformations in CO2-loaded metal–organic framework Zn(MeIm)2 from heat capacity measurements. J. Am. Chem. Soc. *142*, 4833–4841. https://doi.org/10.1021/jacs.9b13883.

Rosi, N.L., Eckert, J., Eddaoudi, M., Vodak, D.T., Kim, J., Keeffe, M., and Yaghi, O.M. (2003). Hydrogen storage in microporous metal-organic frameworks. Science *300*, 1127. https://doi.org/10.1126/science.1083440.

Ryland, A.L. (1958). X-ray diffraction. J. Chem. Educ. *35*, 80. https://doi.org/10.1021/ed035p80.

Sakata, Y., Furukawa, S., Kondo, M., Hirai, K., Horike, N., Takashima, Y., Uehara, H., Louvain, N., Meilikhov, M., Tsuruoka, T., et al. (2013). Shape-memory nanopores induced in coordination frameworks by crystal downsizing. Science *339*, 193–196. https://doi.org/10.1126/science.1231451.

Sheldrick, G.M. (2015). Crystal structure refinement with SHELXL. Acta Cryst. *C71*, 3–8.

Shen, X., Viney, C., Johnson, E.R., Wang, C., and Lu, J.Q. (2013). Large negative thermal expansion of a polymer driven by a submolecular conformational change. Nat. Chem. *5*, 1035–1041. https://doi.org/10.1038/nchem.1780.

Spek, A.L. (2008a). A Multipurpose Crystallographic Tool (Utrecht University).

Spek, A.L. (2008b). PLATON, Multipurpose Crystallographic Tool (Utrecht University).

Spek, A. (2015). Platon SQUEEZE: a tool for the calculation of the disordered solvent contribution to the calculated structure factors. Acta Crystallogr. C *71*, 9–18. https://doi.org/10.1107/S2053229614024929.

Stephens, P.J., Devlin, F.J., Chabalowski, C.F., and Frisch, M.J. (1994). Ab initio calculation of vibrational absorption and circular dichroism spectra using density functional force fields. J. Phys. Chem. *98*, 11623–11627. https://doi.org/10.1021/j100096a001.

Sun, Z., Liu, Q., Qu, G., Feng, Y., and Reetz, M.T. (2019). Utility of B-factors in protein science: interpreting rigidity, flexibility, and internal motion and engineering thermostability. Chem. Rev. *119*, 1626–1665. https://doi.org/10.1021/acs.chemrev.8b00290.

Sun, K., Liu, M., Pei, J., Li, D., Ding, C., Wu, K., and Jiang, H.-L. (2020). Incorporating transition-metal phosphides into metal-organic frameworks for enhanced photocatalysis. Angew. Chem. Int. Ed. *59*, 22749–22755. https://doi.org/10.1002/anie.202011614.

Takashima, Y., Long, D.L., and Cronin, L. (2014). Towards imaging electron density inside metal-organic framework structures. Chem. Commun. *50*, 2271–2274. https://doi.org/10.1039/c3cc48586b.

Tanaka, D., and Kitagawa, S. (2008). Template effects in porous coordination polymers. Chem. Mater. *20*, 922–931. https://doi.org/10.1021/cm7031866.

Vanduyfhuys, L., Rogge, S.M.J., Wieme, J., Vandenbrande, S., Maurin, G., Waroquier, M., and Van Speybroeck, V. (2018). Thermodynamic insight into stimuli-responsive behaviour of soft porous crystals. Nat. Commun. *9*, 204. https://doi.org/10.1038/s41467-017-02666-y.

Wang, Y., Huang, N.Y., Zhang, X.W., He, H., Huang, R.K., Ye, Z.M., Li, Y., Zhou, D.D., Liao, P.Q., Chen, X.M., and Zhang, J.P. (2019). Selective aerobic oxidation of a metal-organic framework boosts thermodynamic and kinetic propylene/propane selectivity. Angew. Chem. Int. Ed. Engl. *58*, 7692–7696. https://doi.org/10.1002/anie.201902209.

Wang, H., Fang, S., Wu, G., Lei, Y., Chen, Q., Wang, H., Wu, Y., Lin, C., Hong, X., Kim, S.K., et al. (2020). Constraining Homo- and Heteroanion Dimers in Ultraclose Proximity within a Self-Assembled Hexacationic cage. J. Am. Chem. Soc. *142*, 20182–20190. https://doi.org/10.1021/jacs.0c10253.

Wu, Q., Niu, M., Chen, X., Tan, L., Fu, C., Ren, X., Ren, J., Li, L., Xu, K., Zhong, H., and Meng, X. (2018). Biocompatible and biodegradable zeolitic imidazolate framework/polydopamine nanocarriers for dual stimulus triggered tumor thermo-chemotherapy. Biomaterials *162*, 132–143. https://doi.org/10.1016/j.biomaterials.2018.02.022.

Yang, L., Qian, S., Wang, X., Cui, X., Chen, B., and Xing, H. (2020). Energy-efficient separation alternatives: metal–organic frameworks and membranes for hydrocarbon separation. Chem. Soc. Rev. *49*, 5359–5406. https://doi.org/10.1039/C9CS00756C.

Yao, Y., Huo, T., Lin, Y.-L., Nie, S., Wu, F., Hua, Y., Wu, J., Kneubehl, A.R., Vogt, M.B., Rico-Hesse, R., and Song, Y. (2019). Discovery, X-ray crystallography and antiviral activity of allosteric inhibitors of flavivirus NS2B-NS3 protease. J. Am. Chem. Soc. *141*, 6832–6836. https://doi.org/10.1021/jacs.9b02505.

Yeung, H.H., Wu, Y., Henke, S., Cheetham, A.K., O'Hare, D., and Walton, R.I. (2016). In situ observation of successive crystallizations and metastable intermediates in the formation of metal-organic frameworks. Angew. Chem. Int. Ed. Engl. *55*, 2012–2016. https://doi.org/10.1002/anie.201508763.

Yu, M.H., Space, B., Franz, D., Zhou, W., He, C., Li, L., Krishna, R., Chang, Z., Li, W., Hu, T.L., and Bu, X.H. (2019). Enhanced gas uptake in a microporous metal-organic framework via a sorbate induced-fit mechanism. J. Am. Chem. Soc. *141*, 17703–17712. https://doi.org/10.1021/jacs.9b07807.

Yuan, S., Qin, J.-S., Zou, L., Chen, Y.-P., Wang, X., Zhang, Q., and Zhou, H.-C. (2016). Thermodynamically guided synthesis of mixed-linker Zr-MOFs with enhanced tunability. J. Am. Chem. Soc. *138*, 6636–6642. https://doi.org/10.1021/jacs.6b03263.

Yuan, S., Sun, X., Pang, J., Lollar, C., Qin, J.-S., Perry, Z., Joseph, E., Wang, X., Fang, Y., Bosch, M., et al. (2017). PCN-250 under pressure: sequential phase transformation and the implications for MOF densification. Joule *1*, 806–815. https://doi.org/10.1016/j.joule.2017.09.001.

YÜ, S.H. (1942). Determination of absolute from relative X-Ray intensity data. Nature *150*, 151–152. https://doi.org/10.1038/150151b0.

Zhao, H., Ni, J., Zhang, J.J., Liu, S.Q., Sun, Y.J., Zhou, H., Li, Y.Q., and Duan, C.Y. (2018). A trichromatic MOF composite for multidimensional ratiometric luminescent sensing. Chem. Sci. *9*, 2918–2926. https://doi.org/10.1039/c8sc00021b.

Zhuo, Z., Huang, Y.-G., Walton, K.S., and Sato, O. (2020). Anisotropic thermal expansion in an anionic framework showing guest-dependent phases. Front. Chem. *8*. https://doi.org/10.3389/fchem.2020.00506.

STAR★METHODS

KEY RESOURCES TABLE

REAGENT or RESOURCE	SOURCE	IDENTIFIER
Chemicals, peptides, and recombinant proteins		
Cyanuric chloride	Aladdin	CAS: 108-77-0
Sodium hydroxide	Aladdin	CAS: 1310-73-2
Sodium bicarbonate	Aladdin	CAS: 144-55-8
2-Aminoterephthalic Acid	Aladdin	CAS: 10312-55-7
3-Aminobenzoic acid	Aladdin	CAS: 99-05-8
Acetone	Sigma-Aldrich	CAS: 67-64-1
Ethanol	Aladdin	CAS: 64-17-5
N-N-Dimethylacetamide (DMA)	Aladdin	CAS: 127-19-5
Zinc nitrate hexahydrate ($Zn(NO_3)\cdot 6H_2O$)	Aladdin	CAS: 10196-18-6
hydrochloric acid (HCl, 37%)	Sigma-Aldrich	CAS: 7647-01-0
1-g-150-initial	CCDC	2084019
1-g-200	CCDC	2084020
1-g-290-final	CCDC	2084018

RESOURCE AVAILABILITY

Lead contact

Further information and requests for resources and reagents should be directed to and will be fulfilled by the lead contact, Jian-Jun, Zhang (zhangjj@dlut.edu.cn)

Materials availability

The MOFs were synthesized and characterized according to a reported method with some modifications (Zhao et al., 2018). A more detailed procedure can be found under method details.

Data and code availability

The crystal data of **1-g-150-initial**, **1-g-200**, and **1-g-290-final** have been deposited at the Cambridge Crystallographic Data Centre (CCDC) and are publicly available as of the date of publication. Accession numbers are listed in the key resources table.

This paper does not report original code.

Any additional information required to reanalyze the data reported in this paper is available from the lead contact upon request.

METHOD DETAILS

General

All chemicals obtained were used without further purification. Thermogravimetric analyses (TGAs) experiments were carried out under a nitrogen atmosphere with a heating rate of 10°C/min using a TA-Q50 thermogravimetric analyzer. A Vario EL III Elemental Analyzer was used to analyze the elements of C, H, and N. Powder X-ray diffraction (PXRD) experiments were measured on a D/MAX-2400 X-ray Diffractometer (Cu–Kα radiation, λ = 1.54059 Å). Variable temperature powder X-ray diffraction patterns for samples were obtained in the Empyrean-100 instrument. The powder samples with homogeneous granularity were sealed in a glass capillary of 0.5 mm internal diameter.

The thermal expansion coefficient was calculated by the equation: $\alpha_l = (l-l_0)/(l_0 \times (T-T_0))$, where l_0 is the initial length of the unit cell, T_0 is the initial temperature for collecting diffraction data; l is the length of unit cell collected diffraction data at a changed temperature T.

Synthesis of ligand (H_5L)

The cyanuric chloride (2.3 g, 12.5 mmol) was firstly dissolved in 15.0 mL of acetone, then the solution was added drop-wise to an aqueous solution (50 mL) which contained 2-aminoterephthalic acid (4.5 g, 25 mmol), NaOH (2.0 g, 50 mmol) and $NaHCO_3$ (2.1 g, 25 mmol). The mixture was stirred at 45°C for 3.5 h. The intermediate was precipitated out after adding excess EtOH in above solution, collected by filtration and dried in the air. The intermediate was dissolved in 25 mL H_2O which firstly contained 3-aminobenzoic acid (1.4 g, 10 mmol), NaOH (0.4 g, 10 mmol) and $NaHCO_3$ (0.85 g, 10 mmol). Then the solution was refluxed at 100°C for 15 h. The solution is cooled naturally to room temperature and then acidified with 6 M HCl until pH = 2 to precipitate the product which was collected by filtration, washed with H_2O and EtOH, and dried in a vacuum desiccator to give 11.6 g (81%) of **H_5L** (2,5-(6-(3-carboxyphenylamino)-1,3,5-triazine-2,4-diyldiimino) diterephthalic acid).

Synthesis of $(Me_2NH_2)[Zn_2(L)(H_2O)]\cdot 3DMA\cdot 3H_2O$ (1-g)

The synthesis was carried out following a slightly modified condition based on the previously reported procedure (Zhao et al., 2018). A mixture solution containing 0.04 mmol 2,5-(6-(3-carboxyphenylamino)-1,3,5-triazine-2,4-diyldiimino) diterephthalic acid (H_5L) and 0.04 mmol $Zn(NO_3)_2\cdot 6H_2O$ in DMA/H_2O(2.4 mL/1.6 mL) in a 20 mL scintillation vial was heated at 115°C for 3 d. Homogeneous block single crystals with a size range from 1 to 3 mm were obtained on the wall of the vial.

Synthesis of MOFs in the solvent with various surface tension

The surface tension of the solvent is tunable by controlling the amount of H_2O added. 0.04 mmol 2,5-(6-(3-carboxyphenylamino)-1,3,5-triazine-2,4-diyldiimino) diterephthalic acid (H_5L) and 0.04 mmol $Zn(NO_3)_2\cdot 6H_2O$ is dissolved in 2.4 mL DMA. Then a different amount of H_2O with 0.4, 1.2, 1.4, or 3.0 mL is added to the mixture, respectively. The scintillation vial with the mixture was capped and heated at 115°C for 3 d. Homogeneous block single crystals with a size range from 1 to 3 mm were obtained on the wall of the vial.

Synthesis of 1-e

The fresh-synthesized crystal **1-g** was filtered out from the mother liquor and washed for 2 min with DMA continuously. The dried filter paper was used to blot up the solvent on the crystal surface. The crystal then was evacuated in a vacuum under 80°C holding 10 hours. The sample was naturally cooled to room temperature and the evacuated crystal **1-e** was stored in a dry and sealed sample tube.

The surface tension measurement

The surface tension of the solution was measured by the instrument K12 (Kruss Company) using the Wilhelmy hanging plate method. The surface tension of each solution was the average value of 5 tests within 1 min. After each test, the cuvette was strictly dried, and the platinum plate was cleaned with ethanol, and the platinum plate was fired with an alcohol lamp to remove the ethanol.

Single crystal X-ray crystallography

Data processing, structure solution, and refinement: X-ray intensity data were measured on a Bruker SMART APEX III CCD-based diffractometer (Mo–Kα radiation, λ = 0.71073 Å) using the SMART and SAINT programs. (SMART Data collection software, version 5.629; Bruker AXS Inc.: Madison, WI, 2003. SAINT Data reduction software, version 6.45; Bruker AXS Inc.: Madison, WI, 2003.) The crystal data was resolved by direct methods and further refined by full-matrix least-squares refinements on F2 using the SHELXL-2018 software (Sheldrick, 2015) and an absorption correction was performed using the SADABS program (Sheldrick, 2015). For the refinement of the corresponding crystals, the non-hydrogen atoms were refined anisotropically. Hydrogen atoms were fixed geometrically at calculated distances and allowed to ride on the parent non-hydrogen atoms. Since the $(Me_2NH_2)^+$ counter cations and the disordered solvents (DMA and H_2O) could not be unambiguously modeled, the PLATON/SQUEEZE program (Spek, 2008a, 2008b) was utilized to calculate the solvent disorder area and remove its contribution to the overall intensity data.

Wilson plot, unit cell parameter, correlation coefficient, Fourier synthesis of electron density map, and mosaicity: Wilson plots were generated with PLATON using .ins and .hkl files for Wilson plots (Lee et al., 2018). Unit cell parameter refinements were carried out by integrating diffraction data and updating the matrixes in .p4p files using APEX3 software until the parameters were converged. Correlation coefficients were calculated by XPREP software using .hkl files generated by SADABS. Mosaicity was obtained from the p4p file after integrations with APEX3, where the mosaicity was estimated using averaged reflection shapes in the *xy* plane of the detector. Electron density map in pores was Fourier synthesized using VESTA software (Momma and Izumi, 2011) with .fab files generated after SQUEEZE.

Variable temperature powder X-ray diffraction (VT-PXRD): This experiment was performed on an Empyrean-100 instrument using an Anton Paar TTK-450 in a vacuum (Cu–Kα radiation, λ = 1.54059 Å). The one-way Temperature Rise Test was carried out at temperatures between 150 and 650 K and the Swing Temperature Test was studied from 290 K down to 150 K then heating back to 290 K. Each pattern was recorded within the 5-30° range (2θ) at the corresponding temperature.

Computational details

All calculations were performed by the Materials Studio package. PDFT calculations were performed by the Dmol3 module, (Delley, 1990, 2000) using the generalized gradient approximation (GGA) with the Perdew-Burke-Ernzerhof (PBE) functional and the double numerical plus d-functions (DNP) basis set, TS for DFT-D correction, and the Effective Core Potentials (ECP). The energy, force, and displacement convergence criterions were set as 1×10^{-5} Ha, 2×10^{-3} Ha, and 5×10^{-3} Å, respectively.

The frequency of the binuclear nodes were calculated at the level of B3LYP (Stephens et al., 1994). LANL2DZ (Hay and Wadt, 1985) basis sets were used for metal atom Zn, while the 6-31g* basis sets were taken for other atoms (C, H, N, O) using Gaussian 16 program (Frisch et al., 2016; Liu et al., 2018). The energy was corrected by DFT-D3 dispersion correction method (Grimme et al., 2010).